DOI: 10.1002/anie.201005839

Core–Shell Structures

Synthesis of AuPt Heteronanostructures with Enhanced Electrocatalytic Activity toward Oxygen Reduction**

*Yena Kim, Jong Wook Hong, Young Wook Lee, Minjung Kim, Dongheun Kim, Wan Soo Yun, and Sang Woo Han**

Nanostructured Pt is the most efficient catalyst known for the oxygen reduction reaction (ORR) in polymer electrolyte membrane fuel cells.[1,2] However, Pt suffers from poisoning associated with electrolytes and the hydroxy layer, which limits the ORR kinetics and long-term stability.[3,4] To improve the activity of Pt, morphology control of the Pt particles[4,5] and using Pt-based bimetallic alloy nanoparticles instead of pure Pt as the electrocatalyst[6–9] have been extensively studied for the past decade.

Recently, Pt-based heteronanostructures such as Pt monolayers or sub-monolayers on metal nanoparticles, core–shell nanoparticles, and particle-on-particle nanostructures have been explored to address the activity, durability, and cost of the particles.[3,10–14] For example, Xia and co-workers[3] and Peng and Yang[13] showed that Pt-on-Pd heterostructures exhibited higher electrocatalytic activities and stabilities toward ORR than those of the state-of-the-art Pt/C catalyst. The improved catalytic properties could be attributed to relatively large surface areas and the presence of particularly active facets on Pt nanocatalysts supported on metal nanoparticles.[3] The seed-mediated growth method has been used in the synthesis of such Pt-based heteronanostructures because this technique can enable the formation of metallic nanostructures with precisely controlled morphology and composition.[15–17] The shape of seed and corresponding specific exposed facets has a great influence on the nucleation and growth of the deposited metal and thus determines the structural and catalytic properties of the resultant nanostructures, although most of the previous studies on the Pt-based heterostructured catalysts have relied on the Pt growth on the roughly spherical metal nanoparticles. Herein, we report on the synthesis of heterogeneous bimetallic nanocrystals consisting of Pt multibranches on Au nanocrystal cores with well-defined morphologies (cubes, rods, and octahedra) as illustrated in Scheme 1, and the effect of underlying core geometry on the electrocatalytic activity for the ORR. The reasons for choosing Au nanocrystals as supports for Pt growth are that synthesis protocols for the preparation of shape- and size-controlled Au nanocrystals have been well developed,[18] and the incorporation of Au into Pt catalysts leads to profound enhancement of both electrocatalytic activity and stability.[19–21]

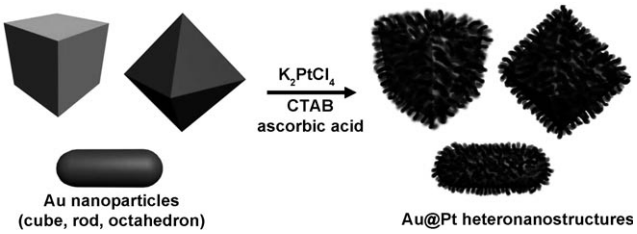

Scheme 1. Synthesis of AuPt bimetallic heteronanostructures consisting of Au nanocrystal cores with well-defined morphologies and dendritic shells of Pt.

In a typical synthesis of AuPt bimetallic heteronanostructures, an aqueous solution of $K_2[PtCl_4]$ was added to an aqueous solution of presynthesized shaped Au nanocrystals such as nanocubes (Au_{cube}), nanorods (Au_{rod}), and nanooctahedra ($Au_{octahedron}$) (see Experimental Section and Figure S1 in the Supporting Information). To this solution, an aqueous solution of cetyltrimethylammonium bromide (CTAB) and ascorbic acid was added, and the mixture was heated at around 100 °C for about 6 min. Representative transmission electron microscopy (TEM; Figure 1 a–c) and scanning electron microscopy (SEM; Figure S2 in the Supporting Information) images of the prepared samples demonstrate the successful preparation of dendritic nanoparticles. The high-angle annular dark-field scanning TEM (HAADF-STEM) images (Figure 1 d–f) and the line profiles of the composition on each single bimetallic particle measured by energy-dispersive X-ray spectroscopy (EDS; Figure 1 g–i) show that the core–shell nanostructures consist of the Au nanocrystals as cores and dendritic shells of Pt, wherein multiple Pt branches have grown on the Au seeds into dendritic tendrils. Elemental mappings of Au and Pt (Figure 1 j–l) also reveal the Au@Pt core–shell structure. UV/Vis spectra of Au@Pt core–shell nanostructures display that the surface plasmon resonance peaks associated with the dipole

[*] J. W. Hong, Y. W. Lee, M. Kim, D. Kim, Prof. S. W. Han
Department of Chemistry and KI for the NanoCentury, KAIST
Daejeon 305-701 (Korea)
Fax: (+82) 42-350-2810
E-mail: sangwoohan@kaist.ac.kr
Homepage: http://ntl.kaist.ac.kr
Y. Kim, Dr. W. S. Yun
Division of Advanced Technology
Korea Research Institute of Standards and Science
Daejeon 305-600 (Korea)

[**] This work was supported by the Basic Science Research Program (KRF-2008-313-C00415, 2008-0062042, 2010-0029149), the Future-based Technology Development Program (Nano Fields) (2009-0082640), and the PRC Program (2009-0082813) through the National Research Foundation (NRF) funded by the Korean government (MEST).

Supporting information for this article is available on the WWW under http://dx.doi.org/10.1002/anie.201005839.

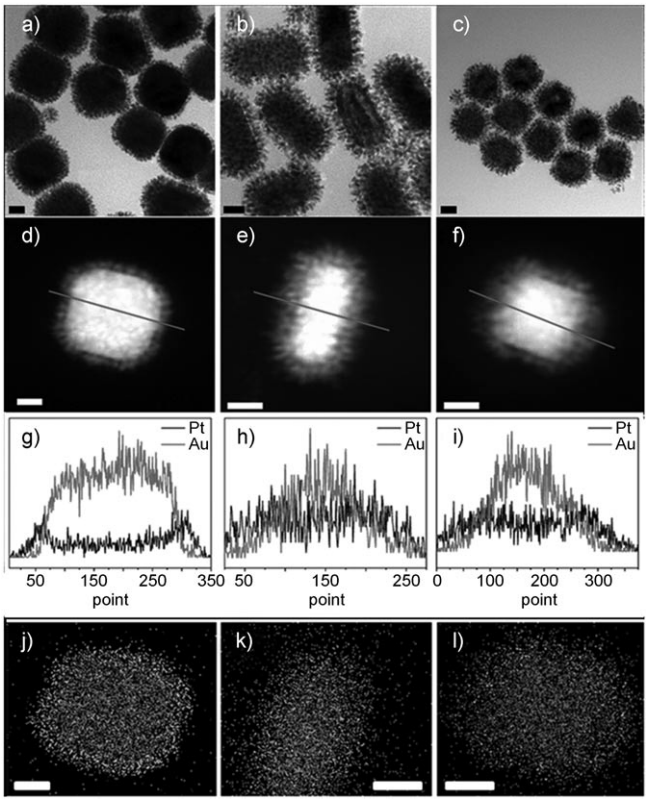

Figure 1. TEM images (a–c), HAADF-STEM images (d–f), cross-sectional compositional line profiles (g–i), and HAADF-STEM-EDS mapping images (j–l) of the Au_{cube}@Pt (left panels), Au_{rod}@Pt (center panels), and $Au_{octahedron}$@Pt (right panels). The scale bars are 20 nm.

resonances of the Au cores are completely damped out by the deposition of Pt (Figure S3 in the Supporting Information). This result could be due to the significantly lower conductivity of Pt at optical frequency than that of Au, indicating the effective formation of Pt dendritic shells.[22] Inductively coupled plasma atomic emission spectroscopy (ICP–AES) analyses showed that the actual molar percentage of Pt in the prepared particles was 33.8, 34.2, and 44.0% for nanocubes, nanorods, and nanooctahedra, respectively, used as cores. The average thicknesses of the Pt shells are 9.3, 7.2, and 7.8 nm for Au_{cube}@Pt, Au_{rod}@Pt, and $Au_{octahedron}$@Pt nanocrystals, respectively. The thickness of the Pt shell can be controlled by variation of the concentration of the Pt precursor. For example, when the concentration of Pt precursor was decreased by half, the average Pt shell thicknesses were decreased to 4.8, 4.1, and 5.2 nm for Au_{cube}@Pt, Au_{rod}@Pt, and $Au_{octahedron}$@Pt nanocrystals, respectively (Figure S4 in the Supporting Information).

Owing to the small difference in lattice parameters between Au and Pt (about 4%), the growth of heterogeneous structures is thermodynamically favored,[23] and the formation of dendritic Pt shells on Au nanocrystals indicates that the nucleation and growth of Pt follow either Volmer–Weber (island growth) or Stranski–Krastanov (island-on-wetting layer growth) growth modes.[10,23,24] In this work, Au nanocrystals with well-defined morphologies were used as the supports for Pt growth. According to their shapes, nanocubes are bound by {100} surfaces and nanorods are enclosed mainly by both {100} and {110} surfaces. Octahedral nanocrystals are exclusively bound by {111} surfaces.[25] Because the difference in lattice parameters and interplay between interfacial energy and surface energies of overlayer and substrate metals are the key factors for determining the growth modes, using different Au cores with different crystalline surfaces could affect the outcome of Pt growth. To investigate the initial growth of the Pt shell, the Au@Pt nanostructures were prepared by using much lower concentration of Pt precursor than that used in the preparation of nanostructures shown in Figure 1. Close inspection of high-resolution TEM (HRTEM) images of bimetallic nanocrystals prepared with low concentration of Pt precursor (25% of the original concentration) revealed the formation of Pt islands on the Au surfaces (Figure 2). Well-

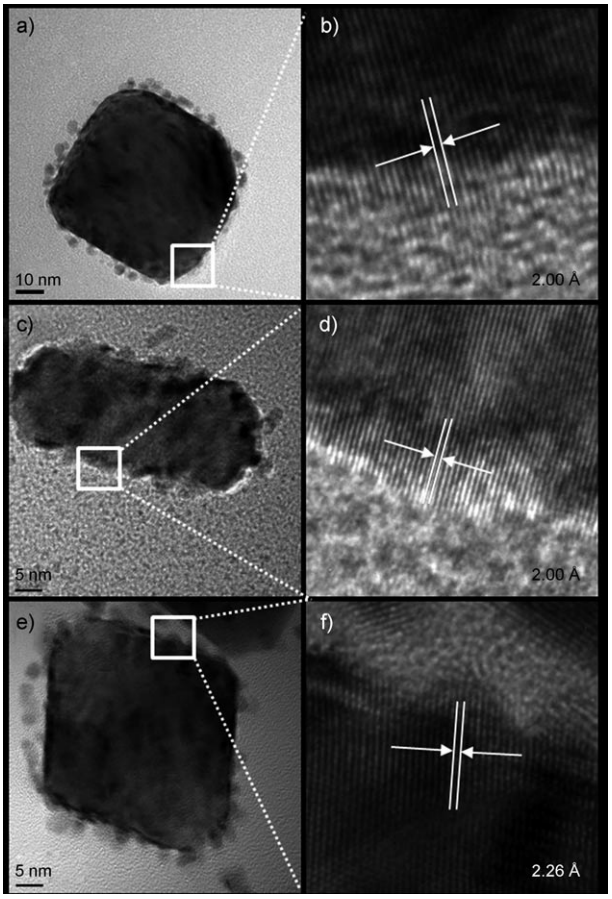

Figure 2. Low- (left panels) and high-magnification (right panels) HRTEM images of Au_{cube}@Pt (a,b), Au_{rod}@Pt (c,d), and $Au_{octahedron}$@Pt (e,f) prepared with a low concentration of Pt precursor.

defined lattice fringes in Pt island regions of Au_{cube}@Pt/Au_{rod}@Pt and $Au_{octahedron}$@Pt nanocrystals correspond mostly to the {100} and {111} surfaces of face-centered cubic Pt, respectively. However, for fully grown Au@Pt nanostructures, stable Pt(111) facets also developed to a large extent for Au_{cube}@Pt and Au_{rod}@Pt nanocrystals (Figure S5 in the Supporting Information). For $Au_{octahedron}$@Pt nanocrystals, {111} surfaces are still dominant in the dendritic Pt shell

(Figure S5 in the Supporting Information). This result was also reflected in the X-ray diffraction (XRD) patterns recorded on the particles; the intensity ratio between the (200) and the (111) diffractions ($I_{(200)}/I_{(111)}$) of Pt for the $Au_{octahedron}$@Pt nanocrystals was much smaller than those of the Au_{cube}@Pt and Au_{rod}@Pt nanocrystals (Figure S6 in the Supporting Information).

The core morphology-dependent electrocatalytic activities of the Au@Pt heteronanostructures toward ORR were investigated, and the results were compared with that of monometallic Pt nanoparticles with dendritic shape (Pt_{den}). The synthesis and structure of Pt_{den} are described in the Experimental Section and Figure S7 in the Supporting Information. Pt_{den} was chosen as the reference because it is a structural analogue for the dendritic Pt shell of Au@Pt heterostructures and it showed efficient electrocatalytic activity for ORR.[26] Figure 3a shows cyclic voltammograms (CVs) of the various catalysts in 0.1 M $HClO_4$. Typical redox peaks associated with the oxidation/reduction of Pt as well as hydrogen adsorption/desorption were observed. The electrochemically active surface areas (ECSA) were calculated by measuring the coulombic charge for hydrogen adsorption.[27] The specific values of ECSA based on the Pt mass for Au_{cube}@Pt, Au_{rod}@Pt, $Au_{octahedron}$@Pt, and Pt_{den} were found to be 102.4, 141.6, 148.1, and 87.7 $m^2 g_{Pt}^{-1}$, respectively (Figure 3b). The higher specific ECSA of Au@Pt nanostructures than Pt_{den} indicate that the formation of heterostructures can provide higher active surface areas despite their larger overall particle size.

The activities of catalysts for oxygen reduction were measured with a rotating-disk electrode (RDE) in O_2-saturated 0.1 M $HClO_4$. The polarization curves for the catalysts are shown in Figure 3c. The current densities (j [mA cm^{-2}]) were normalized to the geometric surface area of the glassy carbon (GC) electrode (0.071 cm^2). Bare Au_{cube}, Au_{rod}, and $Au_{octahedron}$ exhibited no measurable ORR activity under the same experimental conditions (Figure S8 in the Supporting Information). As shown in Figure 3c, the core geometry profoundly affects the activity of the heteronanostructures. The electrocatalytic activities of the different catalysts, estimated from the half-wave potential ($E_{1/2}$),[28] follow the order $Au_{octahedron}$@Pt > Au_{rod}@Pt > Pt_{den} > Au_{cube}@Pt, with $E_{1/2}$ values of 812, 786, 781, and 773 mV versus RHE (reversible hydrogen electrode), respectively. For a better understanding of different ORR activities, the kinetic current (j_k) associated with the intrinsic activity of the catalysts was obtained by a Koutecky–Levich plot for oxygen reduction with different catalysts (experimental details in the Supporting Information).[29] At 0.8 V versus RHE, the mass activities for the $Au_{octahedron}$@Pt, Au_{rod}@Pt, Au_{cube}@Pt, and Pt_{den} catalysts were 215, 128, 82, and 63 mA mg_{Pt}^{-1}, respectively (Figure 3d). Together with the observed most positive $E_{1/2}$ value, this result shows that $Au_{octahedron}$@Pt nanocatalysts drastically outperformed other Au@Pt nanocrystals and Pt particles. Furthermore, the area-specific activity of $Au_{octahedron}$@Pt, obtained by normalization of j_k against ECSA, is also highest among the various catalysts (Figure 3d).

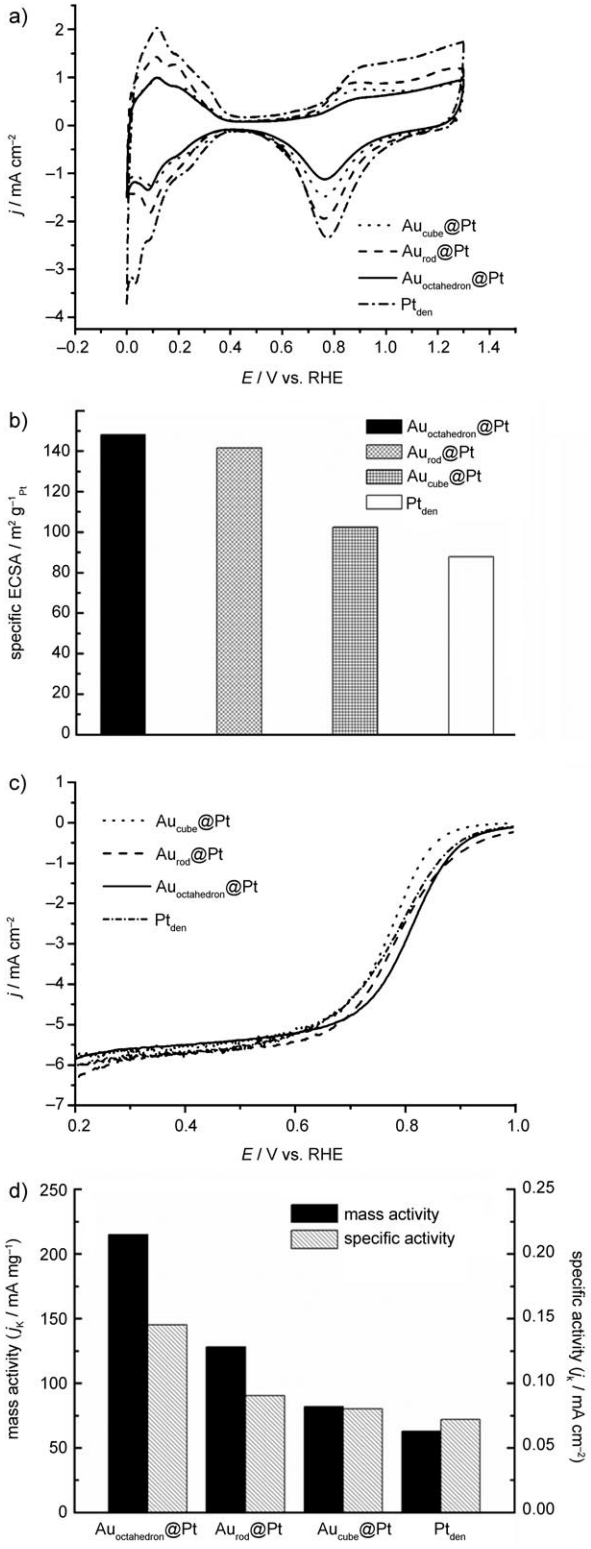

Figure 3. a) CVs of the $Au_{octahedron}$@Pt, Au_{rod}@Pt, Au_{cube}@Pt, and Pt_{den} in 0.1 M $HClO_4$ at a scan rate of 50 mV s^{-1}. The current densities were normalized to the geometric surface area of the GC electrode (0.071 cm^2). b) Specific ECSA for each nanostructure. c) Polarization curves for the $Au_{octahedron}$@Pt, Au_{rod}@Pt, Au_{cube}@Pt, and Pt_{den} nanocatalysts in O_2-saturated 0.1 M $HClO_4$ at a scan rate of 10 mV s^{-1} and a rotation rate of 1600 rpm. d) Mass- and area-specific activity at 0.8 V versus RHE for the various nanocatalysts.

The experimental results demonstrate that Au@Pt heterostructures have higher mass and area-specific activities for ORR than those of monometallic Pt nanodendrites, and their activities highly depend on their core geometries. The choice of octahedral Au nanoparticles as core materials can induce the largest enhancement of the catalytic activity. This improvement could be attributed to the (111)-orientation-rich Pt surface of the $Au_{octahedron}$@Pt crystals. Previous density functional calculations revealed that the moderately compressed Pt(111) facet induced by the difference in lattice parameters is the most effective surface for ORR on nanoparticles because of the slightly decreased oxygen binding energy with respect to that on the extended Pt(111) surface.[12] In fact, the observed lattice spacing on the (111) surfaces of $Au_{octahedron}$@Pt nanocrystals, namely, 2.22 Å, was smaller (−3.9%) than that on the bulk Pt(111) surface (2.31 Å) (Figure S4 in the Supporting Information). Thus, the specific facet of the seed associated with its shape plays a decisive role in the nucleation and growth of the shell and therefore determines the resultant catalytic activity of the heteronanostructures.

The electrochemical stabilities of the catalysts were also investigated by the accelerated durability tests, which were carried out at room temperature in O_2-saturated 0.1 M $HClO_4$ solutions by applying cyclic potential sweeps between 0.6 and 1.0 V versus RHE at a scan rate of 50 mV s^{-1}. Figure 4 shows the CVs of each catalyst before and after 3000 potential cycles. $Au_{octahedron}$@Pt, Au_{rod}@Pt, and Au_{cube}@Pt showed losses of 8.3, 8.4, and 11.1% in ECSA after 3000 cycles, respectively. In contrast to the Au@Pt catalysts, Pt_{den} showed a relatively larger loss of ECSA (23.8%), demonstrating that the AuPt heterostructures had better durability than monometallic Pt nanostructures owing to the incorporation of Au cores.[19–21] The enhanced durability of the Au@Pt catalysts was further confirmed by the TEM and HAADF-STEM-EDS measurements of catalysts after 3000 potential cycles. Although considerable aggregation and sintering of particles were observed for Pt_{den} after the stability test (Figure S9 in the Supporting Information), the morphologies of the Au@Pt catalysts were still maintained after the test, thus resulting in improved catalytic stability (Figures S10–12 in the Supporting Information). However, the relative amounts of Pt were decreased by 5.3, 7.6, and 12.0% after the stability test for $Au_{octahedron}$@Pt, Au_{rod}@Pt, and Au_{cube}@Pt, respectively, which can be correlated with the observed losses of ECSA after the test.

In summary, bimetallic heteronanostructures consisting of a dendritic Pt shell and structured Au cores (nanocubes, nanorods, and nanooctahedra) could be synthesized by a seeded growth method. The Au@Pt nanostructures have exhibited higher electrocatalytic activity and durability for ORR than those of the monometallic Pt catalyst, indicating that the formation of heterostructures can provide higher active catalytic surfaces. Interestingly, the ORR activities are highly dependent on the shape of the cores. The usage of Au nanooctahedron core resulted in the largest improvement of the ORR activity. Our data thus reveal the importance of the core structure for further enhancing the activity of core–shell type nanocatalysts. This method can be extended to other

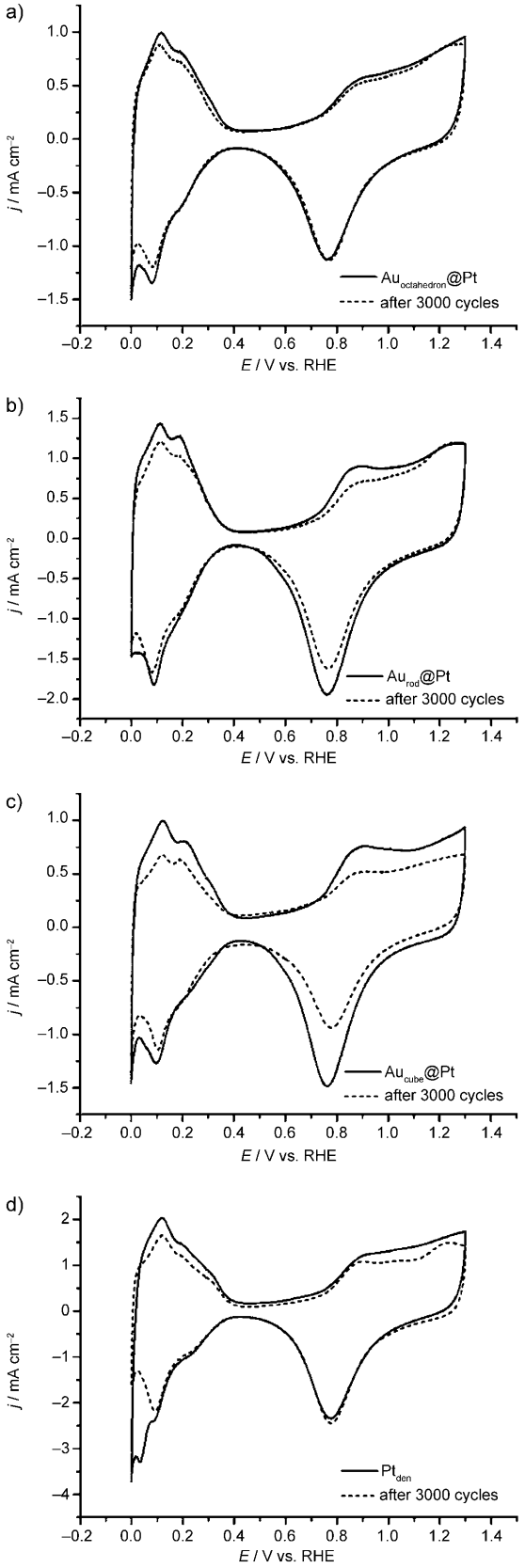

Figure 4. CVs in 0.1 M $HClO_4$ for a) $Au_{octahedron}$@Pt, b) Au_{rod}@Pt, c) Au_{cube}@Pt, and d) Pt_{den} before and after durability test. Scan rate: 50 mV s^{-1}. The current densities were normalized to the geometric surface area of the GC electrode (0.071 cm^2).

metal systems, and further improving the catalytic performance and applying it to other catalytic reactions can be expected through tailoring of the morphology and composition of the nanocrystals.

Experimental Section

$HAuCl_4$ (Aldrich, 99.9%), $K_2[PtCl_4]$ (Aldrich, 98%), ascorbic acid (Sigma, 99.5%), and CTAB (Aldrich, 95%) were used as received. Other chemicals, unless specified, were reagent grade, and Milli-Q water with a resistivity of greater than 18.3 MΩ cm was used in the preparation of aqueous solutions.

In a typical synthesis of Au@Pt core–shell nanocrystals, aqueous Au nanocrystal seed solution (0.6 mL, see the Supporting Information) and 5 mM aqueous $K_2[PtCl_4]$ (0.2 mL) were added to highly purified water (47 mL). To this solution, 10 mM CTAB solution (1 mL) was added. After 5 s, aqueous ascorbic acid (100 mM, 1 mL) was injected quickly into the mixed solution with vigorous stirring, and the solution was stirred further for 1 min. The solution was then heated on a hotplate at approximately 100 °C for around 6 min. The resultant Au@Pt hydrosol was subjected to centrifugation (8000 rpm for 6 min) to remove excess reagents.

The extinction spectra were recorded with a UV/Vis absorption spectrometer (Agilent 8453). SEM images of the samples were taken with a field-emission scanning electron microscope (HITACHI Model S-4800). TEM images and EDS data were obtained with a JEOL JEM-2010 transmission electron microscope operating at 200 kV after placing a drop of hydrosol on carbon-coated Cu grids (200 mesh). HRTEM and HAADF-STEM characterizations were performed with a FEI Technai G2 F30 Super-Twin transmission electron microscope operating at 300 kV. The effective electron probe size and dwell time used in HAADF-STEM-EDS mapping experiments were 1.5 nm and 200 ms per pixel, respectively. The compositions of AuPt bimetallic nanoparticles were determined by ICP–AES (ELAN 6000, Perkin–Elmer). XRD patterns were obtained with a Bruker AXS D8 DISCOVER diffractometer using $Cu_{K\alpha}$ (0.1542 nm) radiation.

Electrochemical measurements were carried out in a three-electrode cell using a CH Instrument Model 760D bipotentiostat. The nanocrystal-modified GC electrode served as a working electrode. Pt wire and Ag/AgCl were used as the counter and reference electrodes, respectively. Details for electrochemical measurements are provided in the Supporting Information. All the potentials are reported with respect to RHE and all electrochemical data were obtained at room temperature.

Received: September 17, 2010
Published online: November 25, 2010

Keywords: nanoparticles · nanostructures · oxygen · platinum · reduction

[1] B. C. H. Steele, A. Heinzel, *Nature* **2001**, *414*, 345.
[2] N. P. Brandon, S. Skinner, B. C. H. Steele, *Annu. Rev. Mater. Res.* **2003**, *33*, 183.
[3] B. Lim, M. Jiang, P. H. Camargo, E. C. Cho, J. Tao, X. Lu, Y. Zhu, Y. Xia, *Science* **2009**, *324*, 1302.
[4] a) C. Wang, H. Daimon, T. Onodera, T. Koda, S. Sun, *Angew. Chem.* **2008**, *120*, 3644; *Angew. Chem. Int. Ed.* **2008**, *47*, 3588; b) C. M. Sánchez-Sánchez, J. Solla-Gullón, F. J. Vidal-Iglesias, A. Aldaz, V. Montiel, E. Herrero, *J. Am. Chem. Soc.* **2010**, *132*, 5622.
[5] C. Wang, H. Daimon, Y. Lee, J. Kim, S. Sun, *J. Am. Chem. Soc.* **2007**, *129*, 6974.
[6] V. R. Stamenkovic, B. S. Mun, K. J. J. Mayrhofer, P. N. Ross, N. M. Markovic, J. Rossmeisl, J. Greeley, J. K. Nørskov, *Angew. Chem.* **2006**, *118*, 2963; *Angew. Chem. Int. Ed.* **2006**, *45*, 2897.
[7] V. R. Stamenkovic, B. S. Mun, M. Arenz, K. J. J. Mayrhofer, C. A. Lucas, G. Wang, P. N. Loss, N. M. Markovic, *Nat. Mater.* **2007**, *6*, 241.
[8] J. Greeley, I. E. L. Stephens, A. S. Bondarenko, T. P. Johansson, H. A. Hansen, T. F. Jaramillo, J. Rossmeisl, I. Chorkendorff, J. K. Nørskov, *Nat. Chem.* **2009**, *1*, 552.
[9] a) J. Kim, Y. Lee, S. Sun, *J. Am. Chem. Soc.* **2010**, *132*, 4996; b) J. Wu, J. Zhang, Z. Peng, S. Yang, F. T. Wagner, H. Yang, *J. Am. Chem. Soc.* **2010**, *132*, 4984; c) Y. Kang, C. B. Murray, *J. Am. Chem. Soc.* **2010**, *132*, 7568.
[10] Z. Peng, H. Yang, *Nano Today* **2009**, *4*, 143.
[11] V. Mazumder, M. Chi, K. L. More, S. Sun, *J. Am. Chem. Soc.* **2010**, *132*, 7848.
[12] J. X. Wang, H. Inada, L. Wu, Y. Zhu, Y. M. Choi, P. Liu, W.-P. Zhou, R. R. Adzic, *J. Am. Chem. Soc.* **2009**, *131*, 17298.
[13] Z. Peng, H. Yang, *J. Am. Chem. Soc.* **2009**, *131*, 7542.
[14] M. Shao, K. Shoemaker, A. Peles, K. Kaneko, L. Protsailo, *J. Am. Chem. Soc.* **2010**, *132*, 9253.
[15] S. E. Habas, H. Lee, V. Radmilovic, G. A. Somorjai, P. Yang, *Nat. Mater.* **2007**, *6*, 692.
[16] D. Seo, C. I. Yoo, J. Jung, H. Song, *J. Am. Chem. Soc.* **2008**, *130*, 2940.
[17] K. Kwon, K. Y. Lee, Y. W. Lee, M. Kim, J. Heo, S. J. Ahn, S. W. Han, *J. Phys. Chem. C* **2007**, *111*, 1161.
[18] M. Grzelczak, J. Pérez-Juste, P. Mulvaney, L. M. Liz-Marzán, *Chem. Soc. Rev.* **2008**, *37*, 1783.
[19] J. Zhang, K. Sasaki, E. Sutter, R. R. Adzic, *Science* **2007**, *315*, 220.
[20] J. Zeng, J. Yang, J. Y. Lee, W. Zhou, *J. Phys. Chem. C* **2006**, *110*, 24606.
[21] S. Zhou, K. McIlwrath, G. Jackson, B. Eichhorn, *J. Am. Chem. Soc.* **2006**, *128*, 1780.
[22] Y. W. Lee, M. Kim, Z. H. Kim, S. W. Han, *J. Am. Chem. Soc.* **2009**, *131*, 17036.
[23] Z. Peng, H. Yang, *Nano Res.* **2009**, *2*, 406.
[24] F.-R. Fan, D.-Y. Liu, Y.-F. Wu, S. Duan, Z.-X. Xie, Z.-Y. Jiang, Z.-Q. Tian, *J. Am. Chem. Soc.* **2008**, *130*, 6949.
[25] G. H. Jeong, M. Kim, Y. W. Lee, W. Choi, W. T. Oh, Q.-H. Park, S. W. Han, *J. Am. Chem. Soc.* **2009**, *131*, 1672.
[26] L. Wang, Y. Yamauchi, *Chem. Mater.* **2009**, *21*, 3562.
[27] The value of ECSA was estimated by the equation ECSA = Q_o/q_o, where Q_o is the surface charge that can be obtained from the area under the CV trace of hydrogen adsorption and q_o is the charge required for the adsorption of a monolayer of hydrogen on the Pt surface (210 μC cm^{-2}).
[28] T. Ghosh, M. B. Vukmirovic, F. J. DiSalvo, R. R. Adzic, *J. Am. Chem. Soc.* **2010**, *132*, 906.
[29] A. J. Bard, L. R. Faulkner, *Electrochemical Methods: Fundamentals and Applications*, Wiley, New York, **2000**.

